Influence of Friction Stir Weld Parameters on the Corrosion Susceptibility of EN AW-7075 Weld Seam and Heat-Affected Zone

Caroline Karina Chandra,* Niklas Sommer, Ben Heider, Marcel Hatzky, Rüdiger Reitz, Stefan Böhm, and Matthias Oechsner

Friction stir welding enables joining of high-strength, lightweight aluminum alloys, e.g., EN-AW-7075, below the melting point by induced plastic deformation. Therefore, heat transfer into the adjacent regions beneath the weld seam is significantly reduced as compared to fusion welding processes such as laser beam welding. However, specific zones along the weld seam area are susceptible to localized corrosion due to grain growth and the precipitation of intermetallic phases. Thus, several approaches toward lowering the corrosion susceptibility of the heat-affected zone are presented. Special interest is given to increasing the plastic deformation by the use of novel multipin welding tools that eventually facilitate reduced heat input during welding as a result of substantially lower tool revolutions. The corrosion behavior is tested by means of full material immersion tests and electrochemical measurements which provide insight into the corrosion kinetics. Using pre- and postmortem microstructural analysis, the mechanisms influencing the initiation of corrosion can be identified. Supported by in-operando temperature measurements, the varied welding parameters and their interrelationships to corrosion resistance can be derived. Furthermore, recommendations on optimal welding parameters to obtain enhanced corrosion resistance can be deduced.

1. Introduction

Friction stir welding (FSW) is becoming increasingly important in many areas of manufacturing technology and is developing into a process that has left the realm of niche applications.

C. K. Chandra, B. Heider, R. Reitz, M. Oechsner
Zentrum für Konstruktionswerkstoffe
MPA-IfW Darmstadt
Technische Universität Darmstadt
Grafenstraße 2, 64283 Darmstadt, Germany
E-mail: caroline_karina.chandra@tu-darmstadt.de

N. Sommer, M. Hatzky, S. Böhm
Trennende und Fügende Fertigungsverfahren
Universität Kassel
Kurt-Wolters-Straße 3, 34125 Kassel, Germany

Particularly from a technological point-of-view, FSW is attractive because joining takes place well below the melting temperature due to severe plastic deformation.[1] This means that temperature-sensitive phenomena such as the emergence of hot cracks are mitigated. As a result, high-strength, precipitation-hardening aluminum alloys, which are generally considered unsuitable for fusion welding, may be welded using FSW.[2,3]

An improved weldability of high-strength aluminum alloys, e.g., the 7000 series, is desirable in lightweight applications such as the aerospace and the automotive sector. Much attention has been dedicated to EN AW-7075, mostly owing to the excellent strength-to-weight ratio. Consequently, this material is extensively used not only in aerospace, defense and military sectors, but also in commercial applications in the automotive and railway industries.[4–6] However, from electrochemical corrosion point-of-view, more comprehensive research and understanding on the interrelationships of welding procedures, precipitation kinetics, and corrosion behavior is necessary. The presence of Mg and Zn has a substantial influence on the corrosion behavior of this alloy.[7] The commonly occurring corrosion types are pitting corrosion, intergranular corrosion (IGC), and stress-corrosion cracking (SCC). These phenomena are strictly related to the occurrence of selective corrosion that emerges due to the heterogeneous nature of the alloy.[8–13] Even in its unwelded state, EN AW-7075 in peak-aged, i.e., T6-condition, exhibits these localized corrosion tendencies for the reason that precipitates and intermetallic phases coexist in the Al-matrix, introducing an imbalance in their electrochemical potentials. Specifically, as some phases behave anodically ($MgZn_2$ and Mg_2Si) and others cathodically (Al_7Cu_2Fe, Al_3Fe, Al_2CuMg) toward the bulk matrix.[8,14] It has been pointed out that exceeding an upper threshold of 4 wt% for Mg + Zn in certain aluminum alloys can render it susceptible to SCC.[15] Additional heat input imposed on the material during the welding process is known to modify the microstructure and the distribution of precipitates along the weld seam and, thus, affecting the overall corrosion resistance of the distinctive weld zones.[16–21] Moreover, the disruption of the T6-condition is also

**ADVANCED
SCIENCE NEWS**

www.advancedsciencenews.com

**ADVANCED
ENGINEERING
MATERIALS**

www.aem-journal.com

expected to degrade its mechanical properties such as ultimate tensile strength (UTS) and microhardness compared to the unaffected base material.[17]

The influence of FSW parameters on different types of aluminum alloys with regard to mechanical and corrosion properties has been widely studied.[22–26] In this context, it has been pointed out that the heat input can be minimized by lowering the rotation speed while, at the same time, maintaining the traverse speed for better corrosion behavior. However, having sufficient frictional heat is crucial for providing the required temperature to influence corrosion behavior positively.[23]

As a result, this work aims to understand process–structure–interrelationships between influential FSW parameters and the corrosion susceptibility of butt-joined EN AW–7075 T6 sheet. Consequently, the study pinpoints to obtain the best corrosion resistance while maintaining the excellent mechanical properties of the alloy.

2. Experimental Section

2.1. Sheet Materials and Welding Procedure

As sheet material, high-strength EN AW-7075 sheet in T6-condition with dimensions of 350 mm × 100 mm × 2 mm was used. The chemical composition of the sheet material was determined by means of energy-dispersive X-ray spectroscopy (EDS; AZtec Oxford), as shown in **Table 1**.

The abutting edges of the sheet were milled to facilitate a reproducible clamping. FSW was performed in depth-controlled mode with a tool tilt angle of 2° on a five-axis FSW machine (PTG Heavy Industries) with a maximum load of 60 kN in z-direction. To vary the degree of plastic deformation, alternating welding tools were employed. The welding tools differ in their respective geometry for single-pin and multipin insertion. The shoulder diameter was 10 mm with a conical 3 mm pin for the single-pin tool. For the multipin welding tool, the shoulder diameter was 12 mm with the same pin diameter as in the single-pin tool, positioned with 2 mm distance in between, creating a stir zone (SZ) with a total width of 12 mm (**Figure 1**).

The goal of preliminary experiments on suitable FSW parameters was a tool rotation to traverse a speed ratio of 1:1. The
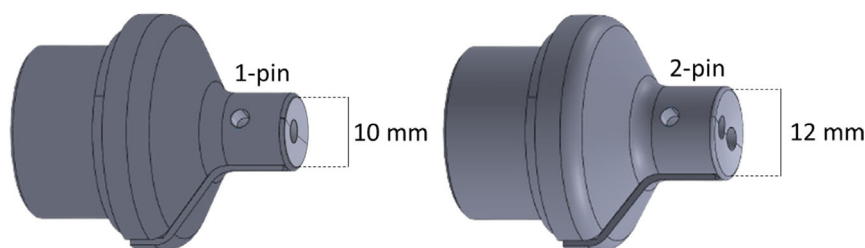
Table 2. Overview of employed FSW welding parameters.

Sample	Tool	Rotation speed [min^{-1}]	Welding speed [mm min^{-1}]	T_{max} [°C]	Tool tilt angle [°]	Tool indentation depth [mm]
A	1-pin	1000	1000	370	2	1.98
B	2-pin	1000	1000	315	2	1.76
C	2-pin	600	1000	297	2	1.76

optimal parameters were elaborated through the use of visual inspection for external irregularities after the welding process according to DIN EN ISO 25239-5. Consequently, the best results were obtained at a welding speed of 1000 mm min^{-1}. Thus, the welding speed was set constant at 1000 mm min^{-1} and the tool was rotated counter-clockwise during all weldments. As a result of the varying tool geometry and plastic deformation, as well as on the basis of previous works on multipin FSW and in-house expertise in the matter, adapted welding parameters were used to reduce the heat input and peak temperatures during the welding process through a further reduction of tool rotation speed, as shown in **Table 2**.[27]

As a result of increased plasticity induced by the multipin tool, the tool rotation speed could be reduced from 1000 to 600 min^{-1}, thus yielding a peak temperature of 297 °C. The temperature was determined using a thermocouple type K attached to the shoulder of the tool.

2.2. Corrosion Testing and Microstructural Characterization

The investigations of corrosion behavior were performed by means of cyclic potentiodynamic polarization (cycpol), immersion test, and neutral salt spray test (NSS). Immersion test and NSS were conducted according to DIN EN ISO 11846:2008-08 and DIN EN ISO 9227:2017, respectively. Subsequent four-point bending tests in chloride-containing medium were carried out with the aim to simulate the occurrence of superimposed corrosion and mechanical loading in the real application of the alloy as a component and thus to investigate the susceptibility of the material system against stress corrosion cracking (SCC).

The purpose of performing cycpol was to assess the overall corrosion kinetics of the representative specimens such as corrosion rate, corrosion potential, and susceptibility to pitting corrosion. The measurement of open circuit potential (OCP) was conducted prior to each cycpol to serve as the corresponding reference point of that particular sample. Further mention of the

Table 1. Chemical composition of EN AW-7075 used in the present study.

| Element	Mg	Si	Ti	Cr	Fe	Cu	Zn	Al
wt%	3.91	0.05	0.10	0.12	0.12	2.05	6.66	86.99

Figure 1. CAD model of welding tool with 1-pin hole and 2-pin hole.

term "vs. OCP" refers to the measured OCP value at 900 s. The stable potential is achieved at this point.[14,28] The scanning rate is constant for both scanning directions, forward and backward scans. The polarization started at a potential of -100 mV versus OCP and was increased with a constant polarization rate of 0.1 mV s^{-1} until a threshold current density of 0.38 mA cm^{-2} is reached. The aforementioned threshold has been chosen based on experiences in prior works with similar material conditions and in compliance with the respective ASTM standards commonly applied in the industry, which state that the threshold should be chosen in such a way that it was at least two orders of magnitude higher than the passive current density.[14,28,29] The potential at the threshold current density is referred as the vertex potential E_V. From this potential value, the scanning direction is reversed. The polarization ended at a potential of -300 mV versus OCP. The observable drastic drops of the current density responses correspond to the first corrosion potential E_{corr} during the forward scan and the second corrosion potential $E_{sec,corr}$ during the backward scan. The difference between both corrosion potentials, $\Delta E_{corr} = E_{corr} - E_{sec,corr}$, as well as the area of the hysteresis loop, was used to predict the probability of pitting corrosion.[29] A silver/silver-chloride (Ag/AgCl) with a potential of $+201$ mV$_H$ with respect to the standard hydrogen electrode (SHE), a platinum mesh, and the sample itself formed a three-electrode assembly as reference electrode (RE), counter electrode (CE) and the working electrode (WE), respectively (**Figure 2**a). The sample holder was made of copper coated with an inert polyether-ether ketone (PEEK). The measurement area was limited to the area of optically visible weld seam in its unground as-received state (with visible welding rings). This electrochemical experiment was conducted in 600 mL of mild saline solution (0.1 wt% NaCl) with a pH of ≈ 5.4 and electrical conductivity of 2.0 mS cm^{-1}. The experiment was controlled by a potentiostat

Reference 600 Gamry Instruments with a sample rate of 1 s for both, OCP and cycpol. Each measurement was repeated three times to ensure reproducibility.

The immersion test conducted according to DIN EN ISO 11846:2008-08 in harsh environment (electrolyte containing 3 wt% NaCl + 1 vol% HCl, pH of 0.5, electrical conductivity of 145 mS cm^{-1}, at room temperature for 24 h) was carried out to determine the resistance to intergranular corrosion of solution heat-treatable aluminum alloys; in this case, the corrosion susceptibilities of different zones coexisting in a welded sample. The state of the sample surface was "as-received," and the back and the side of the sample were protected from electrolyte contact using galvanic tape (Figure 2b). The exposed area of the sample had the dimension of 25 mm × 50 mm (parallel × perpendicular to welding direction) and the electrolyte volume was 200 mL. The exposed to media volume ratio complies with the aforementioned DIN standard. The highly corrosive medium was expected to accelerate the occurrence of contact corrosion in the interface of each zone. The immersion tests were repeated two times.

NSS was conducted in a salt spray test chamber from SC1000 Weiss Umwelttechnik GmbH with a test chamber volume of 950 L. In accordance with DIN EN ISO 9227:2017, the applied electrolyte was 5 wt% NaCl. The test was conducted for 28 days, as opposed to the standard 7-day test, to examine the long-term behavior of the alloy. The documentations of the sample state were conducted at 5 h, 1 day, 2 days, 3 days, 5 days, 7 days, 14 days, 21 days, and 28 days. The sample surface was in its as-received state with its back and side isolated from air contact using galvanic tape. The exposed area was 25 mm × 50 mm (parallel × perpendicular to welding direction).

SCC was conducted for 14 days and carried out distance-controlled in a constant temperature of 24 °C by means of four-point bending test immersed in 200 mL electrolyte containing 1 wt% NaCl (pH of 5.6, electrical conductivity of
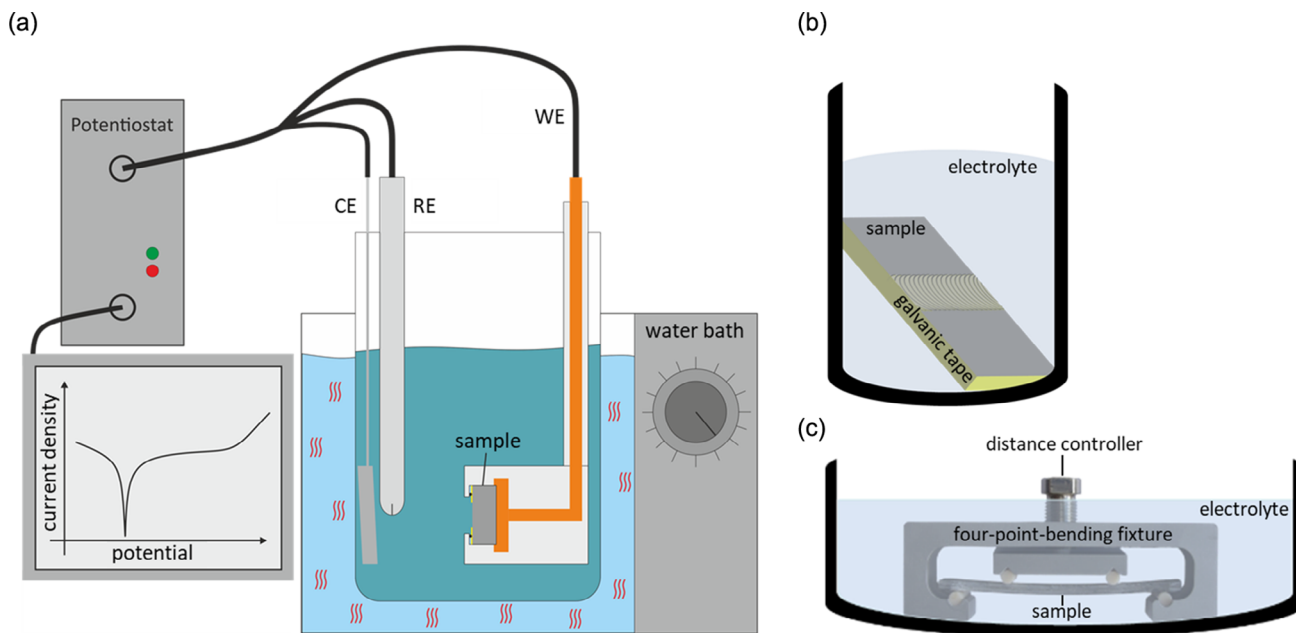

Figure 2. Schematic image of the experimental setup of the a) electrochemical cell, b) immersion test, and c) SCC test.

15.6 mS cm^{-1}) (Figure 2c). The prestresses were set to represent 100% and 135% of the respective yield strength (YS) of each sample. The YS was measured in a tensile test prepared and conducted according to DIN EN ISO 6892-1 (equivalent to ASTM E8M) with four repetitions and converted to deflection distance in the four-point bending test assembly according to DIN EN ISO 7539-2:1995. The sample geometry measured 10 mm × 70 mm × 2 mm in its as-received state and was cleaned ultrasonically in Acetone for 5 min immediately before the experiment. The local hardness measurement was performed using nanoindentation ASMEC Advanced Surface Mechanics UNAT with a load of 100 mN, which allows the measurement of the indentation hardness profile over the cross-section of the sample. The sample preparation and hardness measurement were conducted in fast hardness mode according to DIN EN ISO 14577:2015. The distance of each point was 250 μm. The line mapping was performed twice on each sample.

Microscopic evaluation of the specimen's surficial appearance and topographical top-view images was conducted with a digital light microscope (Keyence VHX-6000). The cross-sections were prepared for subsequent metallographic analyses. The analyses were done using a digital light microscope (Leica Aristomet). EDS analysis was performed using the setup mentioned beforehand (AZtec Oxford) in an SEM (Zeiss EVO MA15) operating at an acceleration voltage of 20 kV.

3. Results and Discussion

3.1. Electrochemical Corrosion

Since the forward polarization was limited by the current density, the difference between E_V and E_{corr} can approximate the overall corrosion resistance and kinetics of the sample surface.[29,30]

Consequently, the lower the kinetics of a corrosion process, the slower the mass loss rate.

All samples exhibit positive hysteresis with their $E_{sec,corr}$ being more negative than their respective E_{corr} (**Figure 3**). Positive hysteresis accompanied by a shift of corrosion potential to more negative values is a strong indicator of a high propensity to the occurrence of pitting corrosion. The size of the positive hysteresis loop, i.e., the difference between forward and backward scan potential-specific current density corresponds to the degree of difficulty for the restoration of the damaged passive film. The disruption of passive film caused by the forward polarization cannot be reversed.[29,31] Comparing the result from sample A (1-pin) and samples B and C (2-pin), potential difference of the E_{corr} of E_V of ≥ 50 mV and approximately 75 mV between sample A and the other samples are observable. Among all samples, sample A exhibits the lowest electrochemical nobility as well as the lowest vertex potential.

Samples A and B do not possess any deflection point during the forward scan between E_{corr} and E_V. In such case, the sample has its equilibrium potential (E_{corr}) and its pitting potential E_{pit} at the same value ($E_{corr} = E_{pit}$), meaning that the lowest potential required for the breakdown of the passive film (occurrence of localized pitting corrosion) is achieved in its currentless state, OCP. Active pitting corrosion is bound to happen spontaneously in this material-electrolyte-arrangement. A pronounced difference between the trend of the cycpol curve of sample C and the other samples is the presence of E_{pit}. It indicates that no spontaneous active corrosion is expected, when the material is exposed to the said electrolyte without the presence of any external current in a simple immersion arrangement. A summary of all measured parameters is depicted in **Table 3**.

The direction of the preferred trend depicts the tendency to a better overall corrosion behavior. A preliminary interpretation of Table 3 shows that while exhibiting the lowest pitting probability
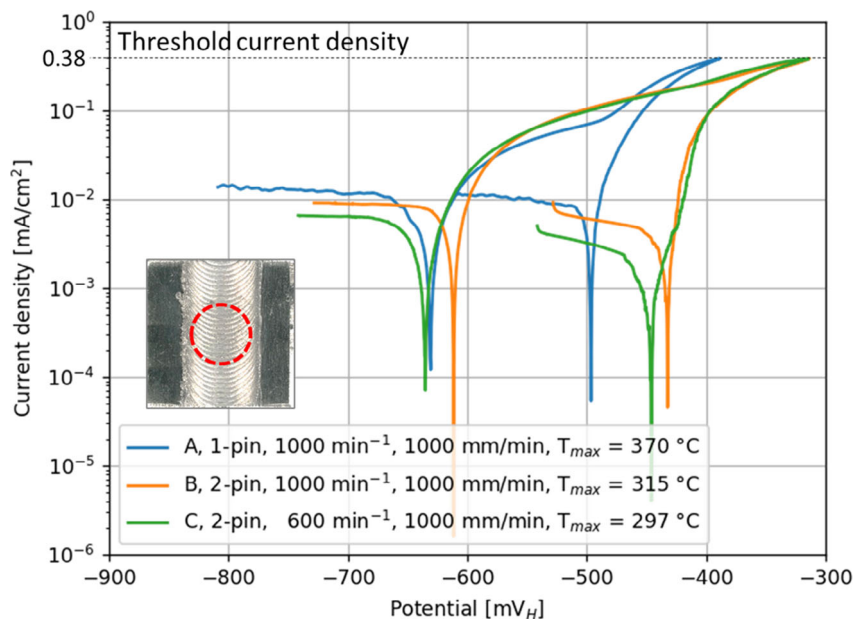
Figure 3. Current density potential curves of samples A, B, and C with threshold current density of 0.38 mA cm^{-2}. Due to the similarity, only one representative curve is shown for each condition.

Table 3. Summary of obtained parameters from cycpol with their respective qualitative preferred trend. Each value represents the arithmetic mean of $n = 3$ independent measurements.

Parameter		A	B	C	Better corrosion resistance when parameter is:
Electrochemical nobility	E_{corr} [mV$_H$]	−497	−433	−447	▲
Pitting probability	ΔE_{corr} [mV]	133	179	187	▼
Potential at threshold current density	E_V [mV$_H$]	−390	−314	−314	▲
Overall corrosion resistance	$E_V−E_{corr}$ [mV]	107	121	135	▲

ΔE_{corr} (133 mV), sample A (1-pin) demonstrates the overall worst behavior. Samples welded using 2-pin tool (samples B and C) have better corrosion behavior compared to sample welded using 1-pin tool and exhibit more or less similar values, regardless of the employed tool revolutions. Taking the presence of the pitting potential in sample C into account, it can be concluded that sample C has the lowest corrosion kinetics compared to samples A and B.

3.2. Immersion Test

The resistance of the samples against IGC was investigated by means of immersion testing. Subsequent documentations of the metallographic cross-sections were prepared for further investigations (**Figure 4**).

As can be derived from the cross-sections, the morphology of the corrosion phenomena on all samples appears similar. The corrosion attack occurs mainly at the weld seam, which extends to the area in its vicinity. Since the area exposed to electrolyte contact includes both, the base metal and weld seam, the absence of corrosive attack at the base metal indicates its action as cathode from electrochemical point-of-view, while the weld seam and its surroundings act as sacrificial anode, hence, forming galvanic corrosion elements. Note that the area of visible weld seam is attributed to the shoulder diameter of the welding tool, which differs for 1-pin and 2-pin tools with 10 and 12 mm, respectively. The difference in the width of extension of corrosion attack in samples B and C can be explained by the corresponding difference in heat input due to reduced tool revolution speed. Accordingly, the lateral extension of the corrosion attack in sample B (rotation speed of 1000 min^{-1}) is wider than for sample C (rotation speed of 600 min^{-1}). Sample B presumably has a wider heat-affected zone (HAZ) compared to sample B. A more detailed documentation from the HAZ in the retreating side (RS) accentuates the corrosion attack, as shown in **Figure 5**. The respective optical micrographs of the HAZ on the advancing side (AS) are very similar and are therefore omitted for clarity.

The IGC attack is more pronounced in sample A than samples B and C. Despite the similar-looking corrosion attack on the optical micrographs HAZ-RS and HAZ-AS, the cross-sections depicted in Figure 4 have clearly shown the asymmetric
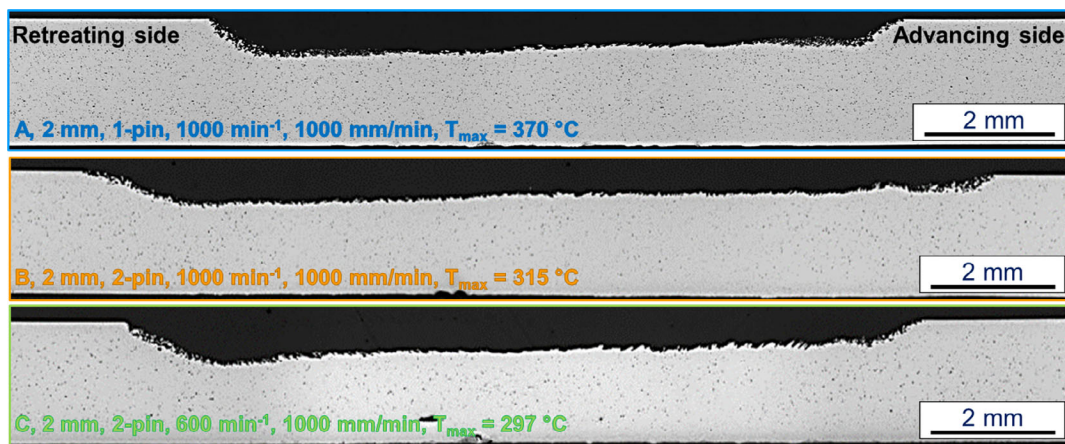

Figure 4. Optical micrographs detailing metallographic cross-sections after immersion tests according to DIN EN ISO 11846:2008-08.
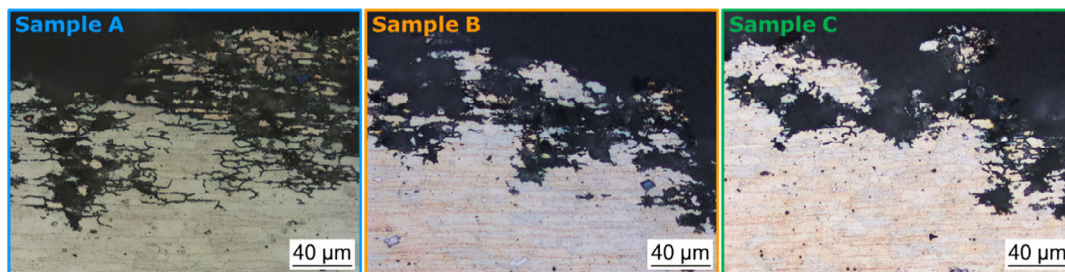

Figure 5. Optical micrographs detailing corrosion attack on the cross-section of HAZ-RS after immersion test (etched using modified Murakami etchant).

**ADVANCED
SCIENCE NEWS**

www.advancedsciencenews.com

**ADVANCED
ENGINEERING
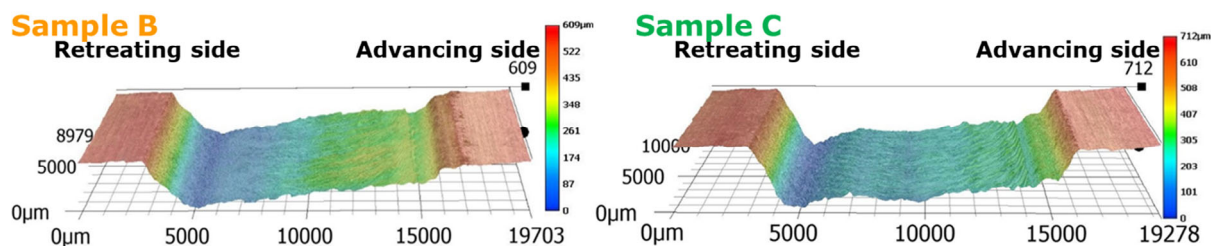MATERIALS**

www.aem-journal.com

Figure 6. Topographic image of samples B and C (top-view).

appearance of the left side and the right side of the weld seam (RS and AS). Asymmetric behavior is a characteristic feature of FSW as opposed to other welding techniques. It is observable from all samples that the attack on the RS is deeper than those of the AS. This effect is verified using the topographic image of the sample (top-view) in **Figure 6**.

Sample C experienced an absolute deeper corrosion attack compared to sample B by $\approx 100\,\mu m$ despite having a lower overall heat input and a lower T_{max} (cf. Table 2). Assuming a perfectly flat initial surface, the area of corrosion attack shown on the cross-section in Figure 4 was measured using the image-processing program ImageJ. The areas are measured for qualitative comparison purposes only. Sample B has an area of material loss of $\approx 5.3\,mm^2$, while sample C is missing $\approx 5.8\,mm^2$ of its area, pinpointing that heat input itself may not be the only influential factor for corrosion resistance.

The cycpol test suggests that sample C proves favorable to sample B with regard to pitting resistance, while the immersion tests indicate contrasting results with regard to corrosion intensity. Keeping in mind that the electrolyte applied in the immersion test is far more aggressive than the one applied in cycpol, both test methods adapt different test conditions and therefore do not allow for direct correlation. However, it can be derived that the benefit to the corrosion behavior gained by reducing the rotation speed and, thus, lowering the heat input, is obviously limited by the contradictory impact of reducing the stirring effect. The latter results in a nonhomogeneous distribution of precipitation in the matrix. Therefore, reducing the stirring effect may cause a higher degree of heterogeneity in the weld seam, thus promoting microgalvanic corrosion within. In fact, the better corrosion behavior of sample B and sample C (2-pin) compared to sample A (1-pin) might be caused by the enhancement of the stirring effect as well. From these results, it can be deduced that the negative impact imposed by reducing the stirring effect can mitigate the benefits of obtaining an overall lower heat input in FSW.

3.3. Salt Spray Test (NSS)

Salt spray tests were conducted for 28 days in total. Samples were assessed at selected time points. No significant changes of the weld surface are observable between 5-h exposure and 28-day exposure. The final state of the sample features a similar appearance to the state of the sample after 5 h, as shown in **Figure 7**.

Subsequent EDS measurements were conducted on the final state of the NSS samples to obtain more information about the accumulation of residue which is mostly found at the transition between weld metal and HAZ (**Figure 8**a).

Based on the EDS results, the assumption that the white residue is the accumulation of salt originating from 5 wt% NaCl salt fog during the test can be eliminated, because the detected amount of Na and Cl in the respective areas is comparatively small (Figure 8b). The change in chemical composition before and after the NSS test on the parent metal close to the visible weld metal area is shown in "Spot 6" and "Spot 6, day 0" in Figure 8b. These results further emphasize that the observed residue between weld metal and HAZ are corrosion products formed by the exposure of the material to salt fog for a prolonged period of time.

The visual appearance of corrosion attack on all samples in their final state is characterized by a high degree of similarity. This finding suggests the immanent behavior of the corrosion morphology, meaning that regardless of the employed FSW parameters, the occurring corrosive attack is similar. These findings suggest that a modification of welding parameters brings little to no influence on the corrosion tests in artificial NSS atmosphere according to DIN EN ISO 9227:2017. Information regarding corrosion initiation points and/or time of the first sign of corrosion with respect to welding parameters cannot be deduced since the appearance of all samples is indistinguishable after a 5-h exposure.
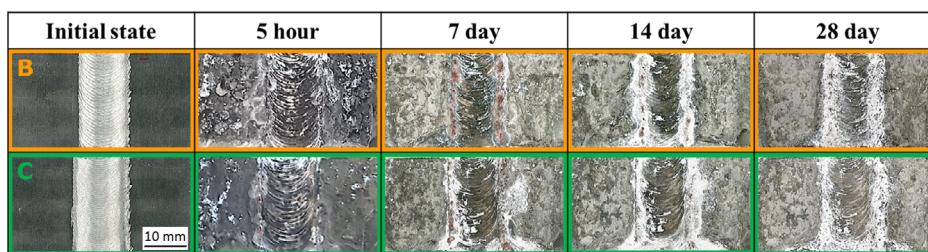

Figure 7. Microscopic images depicting the state of the sample B and sample C during NSS tests in dependence on exposure duration.

(a)

(b)

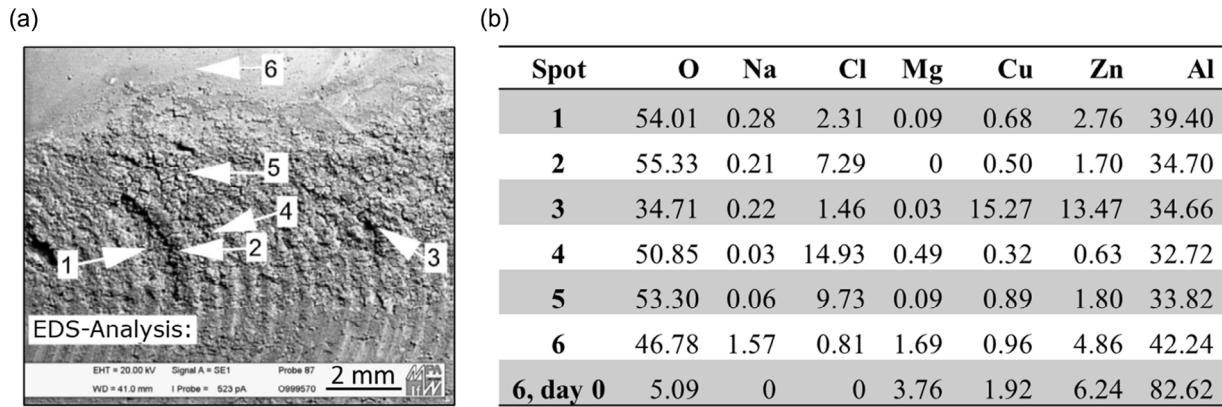| Spot	O	Na	Cl	Mg	Cu	Zn	Al
1	54.01	0.28	2.31	0.09	0.68	2.76	39.40
2	55.33	0.21	7.29	0	0.50	1.70	34.70
3	34.71	0.22	1.46	0.03	15.27	13.47	34.66
4	50.85	0.03	14.93	0.49	0.32	0.63	32.72
5	53.30	0.06	9.73	0.09	0.89	1.80	33.82
6	46.78	1.57	0.81	1.69	0.96	4.86	42.24
6, day 0	5.09	0	0	3.76	1.92	6.24	82.62

Figure 8. a) SEM image showing the location of the corresponding b) EDS measurement on friction stir welded EN AW-7075 (sample A). The chemical composition is given in wt%.

3.4. Stress Corrosion Cracking

There are competing factors that contribute to the SCC susceptibility of EN AW-7075. While high residual tensile stress in the stir zone (SZ) is known to cause material failure in common SCC tests, the HAZ is also known to have a higher tendency to corrosion as compared to the SZ. However, this corrosion susceptibility is—to certain extent—compensated by the residual compressive stresses present in that zone. However, the corrosion damage itself is high enough for deterioration of mechanical properties. Another characteristic of FSW is the asymmetrical corrosion behavior, which was evidenced in Figures 4 and 6. Both alternating damage potentials, residual tensile stress, and overall lower corrosion resistance contribute to material failure under SCC conditions. As the amount of residual tensile stress and the corrosion resistance of the material differ strongly according to their FSW parameters, determining the exact location of the weak point of the welded samples is not trivial.

The applied prestresses are given proportionally to their respective YS. Prior tensile tests were conducted to obtain the YS and Young's modulus E of each sample in its as-received state (**Table 4**).

Table 4. Mechanical properties obtained from tensile test according to DIN EN ISO 6892-1. Each value represents the arithmetic mean of $n = 4$ independent measurements.

	Sample B	Sample C
UTS [MPa]	444 ± 28	484 ± 17
YS [MPa]	419 ± 2	409 ± 2
E [GPa]	71 ± 2	74 ± 9

Sample B with higher rotation speed exhibits a lower UTS (444 MPa) compared to sample C (484 MPa) by ≈10%. This may be attributed to the higher frictional heat input during the FSW process, which, consequently, influences the mechanical properties of the respective joints.[23] However, due to the overlapping standard deviation, the statistical significance has yet to be demonstrated. The failure occurred at the interface between SZ and HAZ-AS for sample B, while sample C exhibited failure in the middle of the SZ (**Figure 9**).

Both failure points can be explained by the presence of metallurgical notches, i.e., abrupt change in local hardness, such as a hardness decrease in the SZ and HAZ, as shown in **Figure 10**. Therefore, the alternating weak spot in the tensile test may be readily explained.

Sample B exhibits a subtle W-form in its hardness profile with a notch to a lower indentation hardness on both sides of the HAZ. These two notches are not observable in the hardness
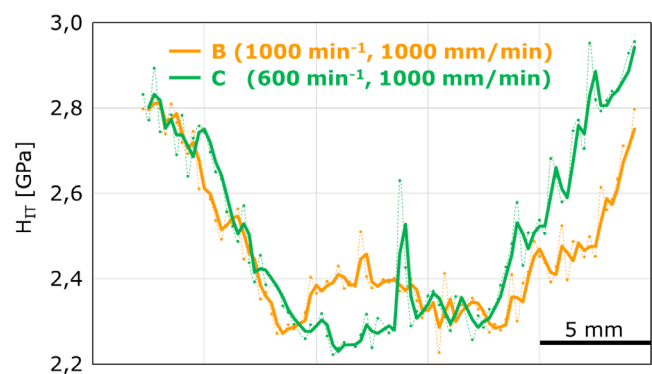

Figure 10. Line mapping of indentation hardness H_{IT} on the cross-section with a load of 100 mN.
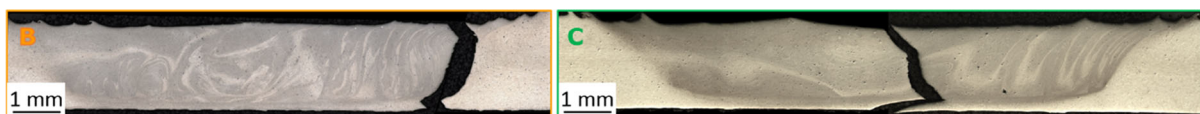

Figure 9. Cross-sections of samples B and C after tensile testing; etched using Keller etchant.
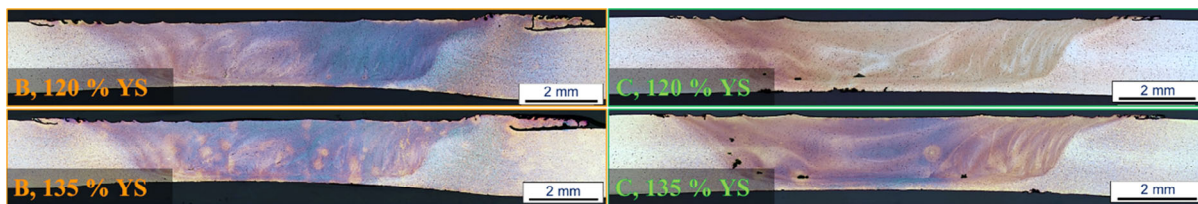
Figure 11. Cross-sections of samples B and C after 14 days of SCC testing. All samples passed without rupture; etched using modified Murakami etchant.

profile of sample C. Instead, a sudden increase in indentation hardness is noticeable in the middle of the weld seam (SZ). In consideration of the respective failure locations of samples B and C, the hardness measurement thus sheds light on the underlying mechanisms. Consequently, the failure of sample B can be attributed to a lower hardness in the HAZ, while the failure of sample C is to be explained by the metallurgical notch imposed by a sudden change of hardness in the middle of the SZ. In light of these results, the crack initiation point in the SCC test is expected to be consistent as well.

Contrary to expectation, the samples do not show any sign of susceptibility against SCC in the said test environment (120% and 135% of respective YS, 14 days RT, 1 wt% NaCl, displacement controlled) (**Figure 11**). One possible explanation for this result is stress relaxation during the 14-day test duration. Another observable finding is that sample C is characterized by pronounced welding defects in the stir zone on the retreating side (Figure 11), which may very well be associated with insufficient material flow and poor mixing due to lower rotational speed.[32] While these defects do not possess a statistically significant and detrimental impact on the measured UTS (cf. Table 4), the presence of welding defects themselves is clearly an undesirable feature.

As the immersion tests suggested, all investigated samples, particularly weld metal and HAZ, are prone to IGC attack, as shown in Figures 4–6. However, it has to be noted that the electrolyte applied in the immersion tests is far more corrosive compared to the one applied during SCC testing. From the obtained SCC results, it can be concluded that the occurrence of intergranular SCC is insignificant under this particular test condition. Further testing is required to determine the threshold at which SCC becomes of significant concern.

4. Conclusion

The aim of the study was to derive a comprehensive understanding on the interrelationships of varying welding parameters during FSW and the corrosion resistance of high-strength EN-AW-7075 T6. The following conclusions can be derived from the results presented and discussed beforehand: 1) The heat input can be significantly reduced by using 2-pin welding tool instead of 1-pin welding tool. Consequently, a reduction of peak temperature from 370 °C to 315 °C under the same rotation and welding speed is rendered possible. 2) The corrosion resistance can be improved by the use of multipin tools yielding a higher degree of plastic deformation, which can be attributed to an enhanced stirring effect. 3) Cycpol tests suggest that samples welded using a 2-pin tool (samples B and C) exhibit a higher

resistance to pitting corrosion compared to the 1-pin sample (sample A). Sample C ($600 \, \text{min}^{-1}$, $1000 \, \text{mm} \, \text{min}^{-1}$) features a slightly better resistance in the currentless state with $E_{\text{pit}} > E_{\text{corr}}$ in contrast to sample B ($1000 \, \text{min}^{-1}$, $1000 \, \text{mm} \, \text{min}^{-1}$) with $E_{\text{pit}} = E_{\text{corr}}$. The difference of E_{V} between 1-pin sample (sample A) and 2-pin samples (sample B and C) is rather significant at 75 mV, indicating that the potential-specific current density of sample A is higher, which leads to more pronounced corrosion kinetics. 4) Immersion tests reveal that sample C underwent a slightly more material loss ($\approx 5.3 \, \text{mm}^2$), as well as a deeper corrosive attack in the vertical direction compared to sample B ($\approx 5.8 \, \text{mm}^2$). Sample B, in contrast, experienced more corrosive attack along the surface in lateral direction (wider HAZ area). 5) NSS tests imply that the corrosion attack is alloy immanent and that there are no major changes observable after 5-h or 28-day exposure time. 6) No crack indication is seen from SCC test within 14 days. Both, samples B and C passed without rupture under the applied test conditions. This finding suggests that SCC is less dominant in this particular test condition. Whether SCC will cause problems in other test scenarios is unclear and, thus, shall be investigated in future studies.

Taking various investigation methods and their results into account, the following essentials can be deduced from this study: 1) The application of 2-pin welding tool has a positive influence on the corrosion resistance. It yields a higher degree of plastic deformation and allows reduction of tool rotation speed, ultimately leading to reduced heat input. 2) Reducing the rotation speed exhibits a certain threshold under which the stirring effect is too low and negates the benefits of lower heat input, proven by sample C (compared to sample B) with many observable welding defects on the cross-sections, as well as the higher corrosion intensity during immersion testing.

A further enhancement of the stirring effect may thus be the most dominant FSW parameter to influence the corrosion behavior. Another reduction of heat input, e.g., by increasing the heat dissipation, is expected to improve the corrosion behavior as well. Consequently, this approach may be suitable to maintain the superior mechanical properties of EN AW-7075 T6 and shall thus be a focus of future research.

Acknowledgements

Conflict of Interest

The authors declare no conflict of interest.

Author Contributions

C.K.C.: Conceptualization, methodology, data curation, investigation, writing-original draft, writing-review & editing; N.S.: Conceptualization, methodology, data curation, investigation, writing-original draft, writing-review & editing; B.H.: Methodology, data curation, investigation; M.H.: Methodology, data curation, investigation; R.R.: Resources, project administration, writing-review & editing, supervision; S.B.: Resources, project administration, writing-review & editing, supervision; M.O.: Resources, project administration, writing-review & editing, supervision.

Data Availability Statement

The data that support the findings of this study are available from the corresponding author upon reasonable request.

Keywords

aa7075, aluminum alloys, corrosion susceptibility, friction stir welding, intergranular corrosion, stress corrosion cracking

[1] M. Lipińska, L. Olejnik, A. Pietras, A. Rosochowski, P. Bazarnik, J. Goliński, T. Brynk, M. Lewandowska, *Mater. Des.* **2015**, *88*, 22.
[2] C. J. Dawes, W. M. Thomas, *TWI Bull.* **1995**, *6*, 124.
[3] C. J. Dawes, W. M. Thomas, *Welding J.* **1996**, *75*, 41.
[4] R. L. Deuis, C. Subramanian, J. M. Yellup, *Compos. Sci. Technol.* **1997**, *57*, 415.
[5] W. S. Miller, L. Zhuang, J. Bottema, A. Wittebrood, P. De Smet, A. Haszler, A. J. M. S. Vieregge, *Mater. Sci. Eng., A* **2000**, *280*, 37.
[6] E. A. Starke, J. T. Staley, *Prog. Aerosp. Sci.* **1996**, *32*, 131.
[7] M. Cabrini, S. Bocchi, G. D'Urso, C. Giardini, S. Lorenzi, C. Testa, T. Pastore, *Materials* **2020**, *13*, 2600.
[8] N. Birbilis, M. K. Cavanaugh, R. G. Buchheit, *Corros. Sci.* **2006**, *48*, 4202.
[9] K.-H. Na, S.-I. Pyun, *Corros. Sci.* **2008**, *50*, 248.
[10] T. Ramgopal, P. I. Gouma, G. S. Frankel, *Corrosion* **2002**, *58*, 687.
[11] F. Andreatta, H. Terryn, J. de Wit, *Electrochim. Acta* **2004**, *49*, 2851.
[12] N. J. H. Holroyd, G. M. Scamans, *Metall. Mater. Trans. A* **2013**, *44*, 1230.
[13] C. A. Loto, R. A. Cottis, *Corrosion* **1989**, *45*, 136.
[14] B. Heider, E. Scharifi, T. Engler, M. Oechsner, K. Steinhoff, *Materialwiss. Werkstofftech.* **2021**, *52*, 145.
[15] S. Kumar, T. K. G. Namboodhiri, *Bull. Mater. Sci.* **2011**, *34*, 311.
[16] R. Nandan, T. Debroy, H. Bhadeshia, *Prog. Mater. Sci.* **2008**, *53*, 980.
[17] T. Venugopal, K. S. Rao, K. P. Rao, *Trans. Indian Inst. Met.* **2004**, *57*, 659.
[18] S. A. Khodir, T. Shibayanagi, *Mater. Sci. Eng., B* **2008**, *148*, 82.
[19] T. Azimzadegan, S. Serajzadeh, *J. Mater. Eng. Perform.* **2010**, *19*, 1256.
[20] M. Navaser, M. Atapour, *J. Mater. Sci. Technol.* **2017**, *33*, 155.
[21] J. B. Lumsden, M. W. Mahoney, C. G. Rhodes, G. A. Pollock, *Corrosion* **2003**, *59*, 212.
[22] B. Murugan, G. Thirunavukarasu, S. Kundu, S. V. Kailas, *Adv. Eng. Mater.* **2019**, *21*, 1800869.
[23] A. Sasikumar, S. Gopi, D. G. Mohan, *Mater. Res. Express* **2021**, *8*, 66531.
[24] M. Lipińska, E. Ura-Bińczyk, L. Olejnik, A. Rosochowski, M. Lewandowska, *Adv. Eng. Mater.* **2017**, *19*, 1600807.
[25] D. G. Mohan, S. Gopi, J. Tomków, S. Memon, *Adv. Mater. Sci.* **2021**, *21*, 67.
[26] D. G. Mohan, S. Gopi, V. Rajasekar, *Indian J. Eng. Mater. Sci.* **2018**, *25*, 203.
[27] M. Hatzky, S. Böhm, *Metals* **2021**, *11*, 1219.
[28] S. V. Sajadifar, T. Suckow, C. K. Chandra, B. Heider, A. Heidarzadeh, J. Zavašnik, R. Reitz, M. Oechsner, P. Groche, T. Niendorf, *J. Manuf. Processes* **2023**, *86*, 336.
[29] S. Esmailzadeh, M. Aliofkhazraei, H. Sarlak, *Prot. Met. Phys. Chem. Surf.* **2018**, *54*, 976.
[30] N. Cotolan, A. Pop, D. Marconi, O. Ponta, L. M. Muresan, *Mater. Corros.* **2015**, *66*, 635.
[31] D. C. Silverman, *Tutorial on Cyclic Potentiodynamic Polarization Technique*, NACE International, Houston, TX **1998**, https://www.osti.gov/biblio/352546.
[32] A. I. Albannai, *Int. J. Sci. Technol. Res.* **2020**, *9*, 318.